Edge photocurrent in bilayer graphene due to inter-Landau-level transitions

Document Version
Submitted manuscript

Link to publication record in Manchester Research Explorer

Edge photocurrent in bilayer graphene due to inter-Landau-level transitions

S. Candussio[1], M.V. Durnev[2], S. Slizovskiy[3,4,6], T. Jötten[1], J. Keil[1], V.V. Bel'kov[2],

J. Yin[3], Y. Yang[3], S.-K. Son[7], A. Mishchenko[3], V. Fal'ko[3,4,5], and S.D. Ganichev[1]

[1]*Terahertz Center, University of Regensburg, 93040 Regensburg, Germany*
[2]*Ioffe Institute, 194021 St. Petersburg, Russia*
[3]*Department of Physics & Astronomy, University of Manchester, Manchester M13 9PL, UK*
[4]*National Graphene Institute, University of Manchester, Manchester M13 9PL, UK*
[5]*Henry Royce Institute for Advanced Materials, Manchester, M13 9PL, UK*
[6]*St. Petersburg INP, Gatchina, 188300, St.Petersburg, Russia and*
[7]*Department of Physics, Mokpo National University, Muan 58554, Republic of Korea*

We report the observation of the resonant excitation of edge photocurrents in bilayer graphene subjected to terahertz radiation and a magnetic field. The resonantly excited edge photocurrent is observed for both inter-band (at low carrier densities) and intra-band (at high densities) transitions between Landau levels (LL). While the intra-band LL transitions can be traced to the classical cyclotron resonance (CR) and produce strong resonant features, the inter-band-LL resonances have quantum nature and lead to the weaker features in the measured photocurrent spectra. The magnitude and polarization properties of the observed features agree with the semiclassical theory of the intra-band edge photogalvanic effect, including its Shubnikov-de-Haas oscillations at low temperatures.

I. INTRODUCTION

The electronic and transport properties of graphene and two-dimensional (2D) semiconductors are strongly dependent on properties of the systems edges. Prominent examples are the quantum Hall regime [1–5], the spin Hall effect in 2D topological insulators [6–11], or quantum valley Hall effects in chiral edge states [5, 12–16]. In general, the energy dispersion and masses of the edge charge carriers can substantially differ from those of the material bulk. Thus, experimental access to these fundamental material properties becomes important. Different experimental techniques have been employed to explore electronic properties of edges including measurements of the quantum Hall effect [17], scanning tunneling microscopy (STM) [18–20], spatially resolved Raman scattering [21–23], spin Hall effect in topological insulator systems [9], imaging of edge currents by superconducting quantum interference devices (SQUID) [24, 25], electron spin resonance [26], high-resolution transmission electron microscopy (TEM) [27], and near-field infrared nanometre-scale microscopy (nanoscopy) [28–32]. In the last decade it has been demonstrated that an access to the spin/valley properties of the edge transport can be obtained employing edge photogalvanic currents excited by terahertz or infrared radiation [33–42]. While detection and analysis of the cyclotron resonance at the edges vicinity would provide informative and important tool to study such edge properties as the energy spectrum, cyclotron mass, carrier density (type), and relaxation times, this challenging goal is missing so far.

Here, we report on the observation of resonantly enhanced edge photogalvanic currents which probe magnetotransport in nanometers-scale vicinity of the edges. The effect is demonstrated in high-mobility μm-scale bilayer graphene structures excited by THz radiation. The peaks in the edge current are caused by absorption peaks at frequencies that match the energies of either intra-band or inter-band Landau level (LL) transitions subject to selection rules and favorable LL occupancy. The stronger intra-band peaks correspond to classical cyclotron resonance (CR), while the weaker inter-band resonances have no classical counterpart. Below, we loosely refer to all the observed peaks as "CR", making clear identification of their origin.

The observed photocurrent flows along the samples edges and its direction is defined by the magnetic field polarity. Upon variation of the magnetic field the edge current behaviour follows the semiclassical shape of the CR in the absorbance. Our analysis of the positions and shape of the CR resonances shows that properties of the edges in studied bilayer graphene samples can be well described by parameters of the material bulk. Depending on the carrier densities the resonance is caused by either inter-band or intra-band transitions between lowest Landau levels at low carrier density or involves transitions between adjacent LL in the conduction band in the semiclassical regime at high carrier densities. In the latter case the resonant edge photogalvanic current additionally exhibits Shubnikov-de-Haas effect related $1/B$-periodic magnetooscillations yielding information on the edge carrier density. Rotating the polarization plane of normally incident THz radiation we observed that orientation of the radiation electric field vector only slightly affects the photocurrent amplitude. The developed microscopic theory of the edge photocurrent in semiclassical regime is based on Boltzmann's kinetic equation and is in a good agreement with the experiment. The effect described here is probed in bilayer graphene; we note, however, that it is of general nature and should be ob-
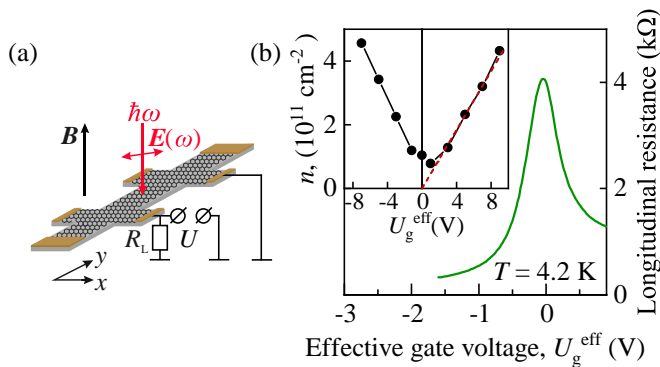
FIG. 1: (a) Sketch of the measurement setup. The photovoltage is measured as a voltage drop U over a load resistor $R_L = 10\,\text{M}\Omega$. (b) Longitudinal resistance versus the effective gate voltage. Corresponding carrier densities are shown in the inset. Dashed line is a linear fit after $n\,[\text{cm}^{-2}] = 0.46 \times 10^{11} U_g^{\text{eff}}$ [V].

servable also in other two-dimensional crystalline systems like monolayer graphene, 2D topological insulators and transition metal dichalcogenide monolayers.

II. SAMPLES AND METHODS

The experiment reported in this paper was carried out on Hall bar structures prepared from exfoliated bilayer graphene, encapsulated in hexagonal boron nitride and equipped with a back gate. Figure 1(b) presents the gate voltage dependence of the longitudinal resistance, demonstrating a clear charge neutrality point (CNP). The CNP slightly shifts for different cool downs, therefore, we introduce an effective gate voltage $U_g^{\text{eff}} = U_g - U_g^{\text{CNP}}$. The carrier densities n as a function of the effective gate voltage obtained from magnetotransport experiments is presented in the inset of Fig. 1.

A continuous wave (cw) optically pumped molecular laser served as source for the normal incident THz radiation exciting the photocurrents in the edges with frequencies of $f = 2.54$ THz (wavelength $\lambda = 118\ \mu$m, photon energy $\hbar\omega = 10.5$ meV) and $f = 0.69$ THz ($\lambda = 432\ \mu$m, $\hbar\omega = 2.85$ meV) [43–45]. These laser lines were obtained using methanol and difluormethane as active media, respectively. A pyroelectric detector was used to control the radiation power on the sample $P \approx 40$ mW. The beam cross-section monitored by a pyroelectric camera had the Gaussian shape with spot sizes at the full width at half maximum (FWHM) of 1.5-2 mm, depending on the frequency. Consequently, the radiation intensity I at the sample was about 2 W/cm^2. The laser used here emits linearly polarized radiation. In our setup the laser radiation electric field vector $\boldsymbol{E}$ was oriented along the y-axis, i.e. along the long side of the Hall bars. To rotate
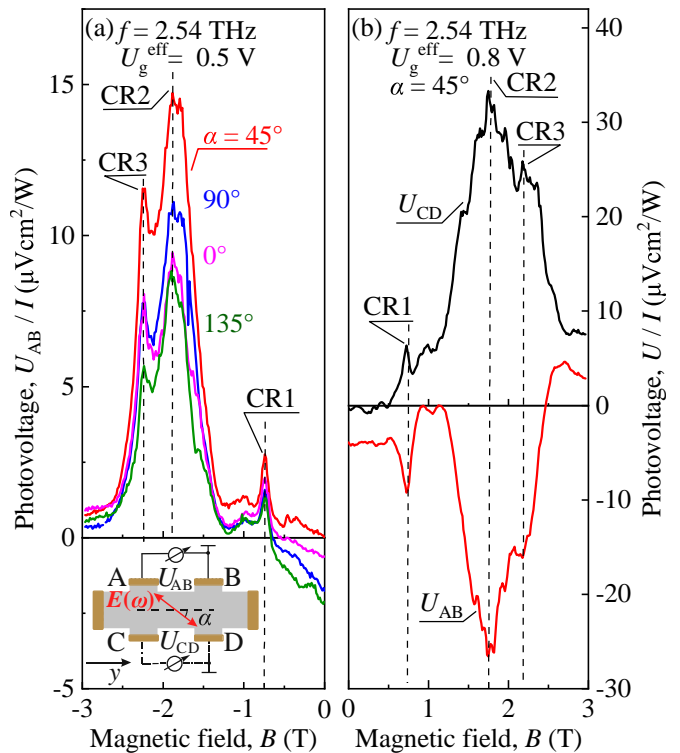

FIG. 2: (a) Magnetic field dependence of the normalized photovoltage $U_{\text{AB}}/I \propto J_{\text{AB}}/I$ measured for different azimuth angles α. The data are presented for the radiation with $f = 2.54$ THz, intensity $I \approx 2$ W/cm^2. Inset shows experimental setup and defines the angle α. CR1, CR2 and CR3 label the resonance positions. (b) Photovoltages U_{AB} and U_{CD} picked up from two contact pairs at the top (red line) and bottom (black line) sample edges aligned along y-axis, see inset.

the electric field in respect to the edges we used crystal quartz $\lambda/2$-plates. The azimuth angle α is the angle between the y-axis and the radiation electric field vector $\boldsymbol{E}$, see inset in Fig. 2(a).

The samples were placed in an optical cryostat and illuminated through z-cut crystal quartz windows. All windows were covered by a thick black polyethylene film, which is transparent in the terahertz range, but prevents uncontrolled illumination of the sample with visible and infrared radiation. The magnetic field B up to 5 T was applied normal to the graphene layer. Experiments were performed at temperature $T = 4.2$ K. A chopper placed in front of the laser modulated the radiation with a frequency of 40 Hz. The generated photocurrents $J \propto U$ were measured as a voltage drop U over a load resistor of $R_L = 10\,\text{M}\Omega$, see Fig. 1(a), applying a standard lock-in amplifier technique.

III. RESONANT EDGE PHOTOCURRENT

Upon exciting the sample with linearly polarized radiation with $f = 2.54$ THz and sweeping the magnetic field we observed three pronounced resonances at fields labeled in Fig. 2 as CR1, CR2, and CR3. The data were detected between contacts located on the long Hall bar edges. Figures 2(a) and (b) show two central observations: (i) the amplitude of the resonance depends on the orientation of the radiation electric field vector with respect to the edges and (ii) signal polarity is consistently opposite for opposite edges. The latter, together with the fact that the signals for opposite edges have almost the same magnitudes, indicates that the signal stems from a photocurrent flowing along the sample edges. The edge contribution $U_{\mathrm{edge}} \propto J_{\mathrm{edge}}$ can be obtained by subtracting the signals measured at the opposite sides, $U_{\mathrm{edge}} = (U_{\mathrm{CD}} - U_{\mathrm{AB}})/2 \propto (J_{\mathrm{CD}} - J_{\mathrm{AB}})/2$.

Figure 3(a) demonstrates that the resonance edge photosignals have opposite signs for opposite polarities of B, i.e. is odd in magnetic field. Varying the Fermi level position by changing the back gate voltage we observed that at moderate gate voltages the CR1 and CR3 become less pronounced in comparison to the CR2, see Fig. 3(b), and at high gate voltages vanish. Positions of CR1, CR2, and CR3 as a function of the carrier density are plotted in Fig. 4(a). When the carrier density changes from 10^{10} to 10^{11} cm^{-2}, only a weak shift of all three resonances is observed.

Changing the radiation frequency from 2.54 to 0.69 THz results in the shift of the CR2 and CR1 by about 3.7 times, which proves that the resonance position scales linearly with f, see Fig. 3(c). Note that for $f = 0.69$ THz the resonance CR3 vanish. As we will show below the resonance positions together with their behaviour upon variation of the carrier density and radiation frequency demonstrate that the resonances are caused by the cyclotron resonances involving transitions between valence and conduction bands (CR1 and CR3) and within the conduction band (CR2).

The data discussed so far were obtained at low gate voltages (below 1.5 V) and, consequently, low carrier densities ($< 0.7 \times 10^{11}$ cm^{-2}). At higher carrier densities the analysis of the CR-induced photocurrent becomes more complicated, because the resonances are superimposed by the SdH-related oscillations in the photocurrent, see Fig. 5. The carrier densities calculated from the period of the $1/B$ oscillations of the photocurrent are the same as those calculated from the corresponding gate voltages. The figure shows, however that the oscillating signal is strongly enhanced at magnetic field of about 1.8 to 2.6 T. The observed enhancement can be satisfactory described assuming a single resonance with a position depending on the carrier density. Our analysis below demonstrates that this behaviour is well described by the density de-
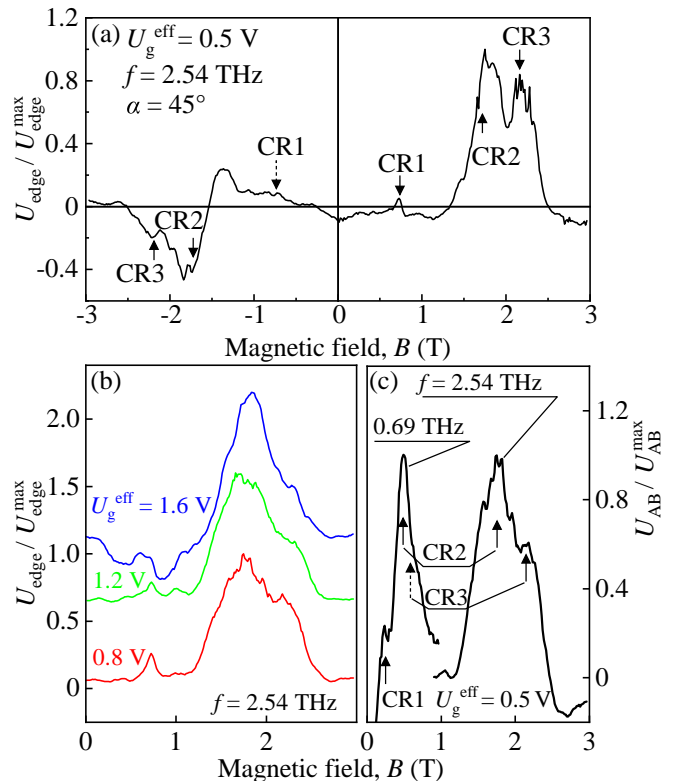

FIG. 3: (a) Magnetic field dependence of the edge contribution of the photovoltage $U_{\mathrm{edge}} = (U_{\mathrm{CD}} - U_{\mathrm{AB}})/2$ normalized to its maximal value $U_{\mathrm{edge}}^{\mathrm{max}}$ corresponding to the resonance CR2. The data are obtained for $f = 2.54$ THz and $\alpha = 45°$. CR1, CR2, and CR3 label the resonance positions. (b) Magnetic field dependence of the normalized edge photovoltage $U_{\mathrm{edge}}/U_{\mathrm{edge}}^{\mathrm{max}}$ measured for different effective gate voltages U_g^{eff}. The curves are vertically shifted by 0.2 for visibility. (c) Magnetic field dependence of the photovoltage U_{AB} normalized to its maximum value $U_{\mathrm{AB}}^{\mathrm{max}}$ corresponding to the resonance CR2. The data are presented for two radiation frequencies $f = 2.54$ and 0.69 THz. CR2 labels positions of the photovoltage maxima, whose position linearly shifts to lower magnetic field by the frequency reduction according $B_{\mathrm{CR2}}(2.54\ \mathrm{THz})/B_{\mathrm{CR2}}(0.69\ \mathrm{THz}) = 2.54/0.69$.

pendence of the cyclotron resonance caused by optical transitions within the conduction band. Note that these results provide an additional evidence for the absence of resonances CR1 and CR3 at high carrier density.

As addressed above, the magnitude of the CR-induced photocurrents changes upon rotation of the radiation electric field vector with respect to the edges, see Fig. 2(a). The dependence of the signal on the azimuth angle α can be well fitted by

$$U \propto J = J_{\mathrm{L}} \sin(2\alpha + \psi) + J_0, \qquad (1)$$

see Fig. 6 for contacts AB (upper edge). Here J_{L} and J_0 are the amplitudes of the polarization dependent and
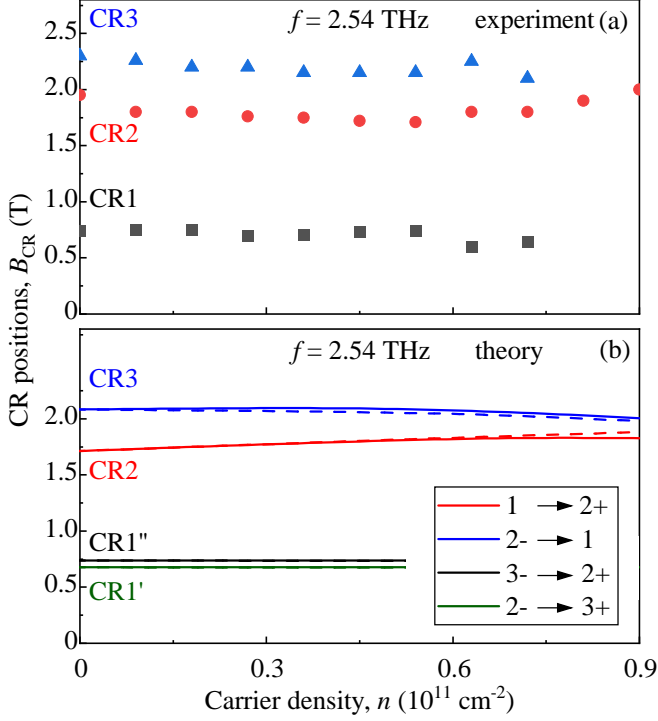
FIG. 4: Dependences of the cyclotron resonance positions B_{CR1}, B_{CR2}, and B_{CR3} on the carrier density $n\,[\text{cm}^{-2}] = 0.46 \times 10^{11} U_g^{\text{eff}}$ [V]. (a) data obtained from the photovoltage resonances. (b) Values calculated from the allowed optical transitions between Landau levels listed in the plot legend. Solid/dashed lines correspond to valleys K^+/K^-. From the position of the CR2 corresponding to transitions within the conduction band we estimate the cyclotron mass m_{CR}, which for zero density is $0.019\,m_0$. It increases with the increase of carrier density due to growth of the asymmetry parameter Δ with the gate voltage, see Eq. (3).

independent contributions, respectively. Note that that for the CR-induced signals the phase shift ψ is almost zero. Furthermore, while, the signal strength varies with the azimuth angle, the sign of the resonance response remains the same and is defined by the magnetic field polarity only.

IV. IDENTIFICATION OF CYCLOTRON RESONANCES

To identify optical transitions responsible for the observed cyclotron resonances we obtain the energy dispersion as a function of the magnetic field of bilayer graphene and consider the corresponding selection rules. Bilayer graphene has a unit cell with 4 carbon atoms, A_1, B_1, A_2, B_2, where A_1 of the top layer lies above B_2 of the bottom layer. The dispersion is described with a Slonczewski-Weiss-McClure tight-binding model pa-

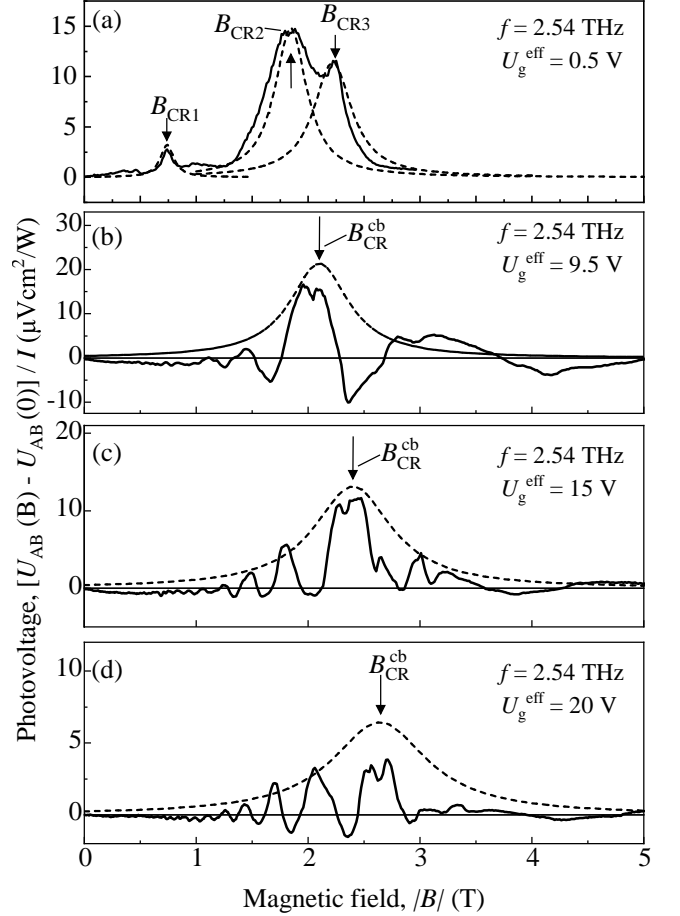FIG. 5: Magnetic field dependence of the photovoltage $[U_{AB}(B) - U_{AB}(0)]$. The data obtained for $\alpha = 45°$ are given for different gate voltages increased from (a) $U_g^{\text{eff}} = 0.5\,\text{V}$ to (d) $U_g^{\text{eff}} = 20\,\text{V}$. Dashed lines show fits after Eq. (4). The values of B_{CR1} (for transitions $2- \rightarrow 3+$ and $3- \rightarrow 2+$) and B_{CR3} (for transitions $2- \rightarrow 1$) used for fits are calculated after Eqs. (2). The values of B_{CR2} and B_{CR}^{cb} are calculated after Eq. (3) for transitions between neighboring Landau levels in the conduction band: $1 \rightarrow 2+$, $2+ \rightarrow 3+$, $4+ \rightarrow 5+$, and $5+ \rightarrow 6+$ in panels (a), (b), (c), and (d), respectively. Vertical arrows indicate the cyclotron resonance positions. The transport broadening parameter $\gamma = 1/\tau = 1.43\,\text{ps}^{-1}$ is obtained from the transport measurements. The used radiative decay parameters Γ are given in Tab. I.

rameterized by [46–48] parameters $\gamma_0 = 3.16\,\text{eV}$ (minus $A_i - B_i$ hoppings), $\gamma_1 = 0.35\,\text{eV}$ ($A_1 - B_2$ hopping), $\gamma_3 = 0.3\,\text{eV}$ (minus $B_1 - A_2$ hopping), $\gamma_4 = 0.14\,\text{eV}$ ($B_1 - B_2$ and $A_1 - A_2$ hoppings), $\Delta_{A_i B_i} = 0.05\,\text{eV}$ (sublattice energy difference $E_{A_1} - E_{B_1}$ and $E_{B_2} - E_{A_2}$) and top-bottom asymmetry parameter $\Delta = \frac{1}{2}(E_{A_1} + E_{B_1} - E_{A_2} - E_{B_2})$ that is induced by a vertical electric displacement field since the field of the bottom gate is not fully screened by the bottom graphene layer. Note that this parameter defines the gap. The resulting 4-band tight-binding model
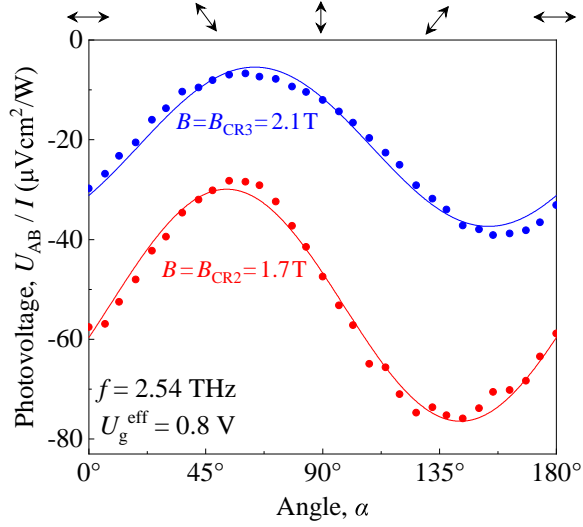
FIG. 6: Dependence of the normailzed photovoltage U_{AB}/I on the azimuth angle α. The data were measured for the magnetic fields B_{CR2} and B_{CR3}. Solid lines are fits after Eq. (1). Arrows on top illustrate states of polarization. Note that at $\alpha = 0$ electric field vector $\boldsymbol{E}$ is oriented parallel to y-axis, i.e. the long side of the Hall bar.

has been used to compute numerically the spectrum of Landau levels and the parameter Δ has been found from self-consistent Hartree approximation that is formulated as [49–51]

$$\Delta = \frac{4\pi e^2 c_0}{\varepsilon}\left[n_2 - \frac{\varepsilon+1}{4}(n_1 - n_2)\right],$$

where $c_0 = 0.335\,\mathrm{nm}$ is the interlayer separation, $\varepsilon \approx 2.7$ accounts for electric polarizability of carbon orbitals in graphene and $n_{1,2}$ (constrained as $n = n_1 + n_2$) are the density of electrons at graphene layers that can be found from the wave functions of occupied Landau levels with phenomenological broadening.

To understand the labeling of Landau levels and gain qualitative understanding of the results we note that the 4-band model can be reduced to an effective 2-band model with Hamiltonian [49, 50, 52]

$$\hat{H}_2 = \hat{h}_0 + \hat{h}_w + \hat{h}_4 + \hat{h}_\Delta + \hat{h}_U,$$
$$\hat{h}_0 = -\frac{1}{2m}\begin{pmatrix} 0 & (\pi^\dagger)^2 \\ \pi^2 & 0 \end{pmatrix},$$
$$\hat{h}_w = v_3\begin{pmatrix} 0 & \pi \\ \pi^\dagger & 0 \end{pmatrix} - \frac{v_3 a}{4\sqrt{3}\hbar}\begin{pmatrix} 0 & (\pi^\dagger)^2 \\ \pi^2 & 0 \end{pmatrix},$$
$$\hat{h}_4 = V_4\begin{pmatrix} \pi^\dagger\pi & 0 \\ 0 & \pi\pi^\dagger \end{pmatrix}, \quad V_4 \equiv \frac{2v_0 v_4}{\gamma_1} + \frac{\Delta_{AB}v_0^2}{\gamma_1^2},$$
$$\hat{h}_\Delta = -\frac{\Delta}{2}\left[\begin{pmatrix} 1 & 0 \\ 0 & -1 \end{pmatrix} - \frac{2v^2}{\gamma_1^2}\begin{pmatrix} \pi^\dagger\pi & 0 \\ 0 & -\pi\pi^\dagger \end{pmatrix}\right],$$

where $\pi = \xi p_x + i p_y$, $v_i = \sqrt{3}a\gamma_i/2\hbar$, $m = \gamma_1/(2v_0^2)$, a is a

lattice constant of graphene and $\xi = \pm 1$ denotes the $K^\pm$ valleys. We note that $\hat{h}_4$ is responsible for electron-hole asymmetry of the spectrum (with holes being slightly more massive), $\hat{h}_w$ is a trigonal warping term and $\hat{h}_\Delta$ is a top-bottom asymmetry term that inevitably arizes in single-gated devices and is responsible for the gap between valence and conduction bands.

In the standard basis of magnetic eigenstates $\varphi_l(x,y) = h_l(x/l_B - p_y l_B/\hbar)e^{ip_y y/\hbar}$, where h_l are harmonic oscillator eigenstates and $l_B = \sqrt{\hbar c/eB}$, the operators π act as lowering operators $\pi\varphi_l = -i\sqrt{2l}(\hbar/l_B)\varphi_{l-1}$ at the valley K^+ and as raising operators in the opposite valley. This allows us to find the spectrum of Landau levels analytically once we neglect the trigonal warping term. In the valley K^+ the spectrum is

$$E_{\pm l} = \frac{2l-1}{l_B^2}\hbar^2 V_4 \pm \frac{\sqrt{l(l-1) + m^2\left(V_4 + l_B^2\Delta/(2\hbar^2)\right)^2}}{\hbar^{-2}l_B^2 m},$$
$$\psi_{l,\pm} \approx \frac{1}{\sqrt{2}}\begin{pmatrix} \varphi_l \\ \pm\varphi_{l-2} \end{pmatrix}, \quad l \geq 2$$
$$E_1 = \frac{\Delta}{2} + \frac{2\hbar^2 V_4}{l_B^2}, \quad \psi_{1\,K_+} = \begin{pmatrix} \varphi_1 \\ 0 \end{pmatrix}$$
$$E_0 = \frac{\Delta}{2}, \quad \psi_{0,\,K_+} = \begin{pmatrix} \varphi_0, \\ 0 \end{pmatrix}. \tag{2}$$

This clarifies the labeling of LLs as $3-, 2-, 0, 1, 2+, 3+$ ..., shown in Fig. 7 ($+/-$ corresponds to Landau levels in conduction/valence band). To calculate LL spectrum for the K^- valley Δ must be substituted by $-\Delta$.

The allowed optical transitions are obtained from the selection rules following Ref. [53]. For the circularly polarized radiation the allowed transitions are

$$(2-) \to (1), \ (3-) \to (2\pm), \ (4-) \to (3\pm)...$$

when $\boldsymbol{B}$ is parallel to the direction of light angular momentum ($B > 0$ in Fig. 7) or

$$...(3\mp) \to (4+), \ (2\mp) \to (3+), \ (1) \to (2+)$$

when $\boldsymbol{B}$ is anti-parallel to the direction of light angular momentum ($B < 0$ in Fig. 7). The energy of $(1) \to (2+)$ and $(2-) \to (1)$ transitions are slightly valley-split when $\Delta \neq 0$, while for other transitions the valley splitting is negligibly small. The transitions $(l-) \to ((l-1)-)$ at $l \gg 1$ correspond to classical CR transitions for holes, transitions $(l+) \to ((l+1)+)$ are classical CR for electrons, while the rest are the quantum inter-band transitions. Note that level (0) does not participate in radiation emission/absorption in case of small asymmetry parameter, see Ref. [53]. The selection rules need to be combined with the conditions that the initial (final) states are, at least partially, filled (empty). At low electron doping and for a frequency of $f = 2.54$ THz these yield four resonances labeled CR1′, CR1″, CR2, and CR3 in Fig. 7. The

calculated positions correspond well to those detected in experiment, see, e.g., Fig. 2. Because CRs are excited by linearly polarized radiation the resonances in Fig. 7 at positive (negative) magnetic fields appear also for negative (positive) B. Note that in experiment the transitions CR1$'$ and CR1$''$ are not resolved because they have very close positions. We also note that the difference in the CR2 and CR3 peak positions is due to electron-hole asymmetry of the spectrum ($\hat{h}_4$ term in Hamiltonian), this results in a larger mass of holes. With the increase of the carrier density the final states for the inter-band transitions in CR3, CR1$'$ and CR1$''$ become occupied and these resonances vanish. This is indeed observed in the experiment, see Fig. 4. The occupation of the final states is also the reason of disappearance of the CR3 resonance at substantial frequency reduction, see Fig. 3(c).

At high densities, the classical regime applies and the distance between the neighboring Landau levels l and $l+1$ for $l \gg 1$, determining the position of CR, is given by

$$E_{l+1} - E_l \approx \frac{2\hbar^2 V_4}{l_B^2}\text{sign}(l) \tag{3}$$
$$+ \frac{\hbar^2}{l_B^2 m \sqrt{1 + m^2 \left(V_4 + l_B^2 \Delta/(2\hbar^2)\right)^2 / l^2}}$$

where we have to keep the term containing Δ since the latter grows almost linearly with increasing doping and hence is important even at large l. The values of resonance magnetic field B_{CR} are calculated using Eq. (2) at low carrier density and Eq. (3) at high carrier density corresponding to the semiclassical regime. The calculated values of B_{CR} were then used to fit the data in Fig. 5. The growth of Δ with gate voltage explains the reduction of LL separation, and, consequently, the growth of B_{CR} with increasing electron density.

Below we show that at cyclotron resonance the edge current flows within a strip with the width equal to the cyclotron diameter ($2v/\omega_c$, where v is the carrier velocity at the Fermi level). This value is around tens of nanometers and is already smaller than the free path length at experimental conditions. Therefore, at CR we probe a few tens of nm wide region near the edge. For low gate voltages, the doping near the edge is the same as in the bulk, so the CR position is determined by the bulk doping level. In general, at higher gate voltages (as used in Fig. 5), the doping may become notably inhomogeneous near the edge of the graphene–back gate capacitor at the scale $d/\epsilon \approx 100$ nm, where $d \approx 400$ nm is the distance to the bottom gate [54, 55] and $\epsilon \approx 4$ is the dielectric constant of SiO$_2$ dielectric. This effect may lead to broadening of the edge current region and to deviations of the CR position from that predicted from the bulk doping. However, carrier densities obtained from the period of the photocurrent oscillations, Fig. 5, coincide with that calculated from the corresponding gate voltages.

Our analysis below demonstrates that the resonant behaviour of the observed edge photocurrents upon variation of the magnetic field follows the semiclassical shape of the CR in the absorbance, given by

$$\eta \propto \sum_{\pm} \frac{1}{(\Gamma + 1/\tau)^2 + (\omega \pm \omega_c)^2} \ . \tag{4}$$

Apart from the conventional transport width of the CR given by the momentum relaxation rate $1/\tau$, here we include an additional electrodynamic contribution, $\Gamma = 2\pi e^2 n/c\,m_{\text{CR}}$, where m_{CR} is the cyclotron mass, which accounts for a significant reflection of the radiation in the vicinity of CR in high density samples [56–58]. The curves calculated after the right-hand side of Eq. (4) are shown by dashed lines in Fig. 5 demonstrating a good agreement with the experimental data. In these plots we used the values of $\tau = 0.7$ ps extracted from the mobility measurements at $U_{\text{g}}^{\text{eff}} = 0.5$ V, the cyclotron electron mass m_{CR} obtained from the calculated CR positions and the radiative decay parameter Γ calculated for different $U_{\text{g}}^{\text{eff}}$, which are summarized in Tab. I. The values of B_{CR} in the low-density regime were calculated after Eq. (2) for the transitions between the lowest Landau levels, see Fig. 5(a) and resonances B_{CR1}, B_{CR2} and B_{CR3}. In the high density regime B_{CR} was obtained from Eq. (3) for the intra-band transitions between the neighboring Landau levels in the conduction band, see $B_{\text{CR}}^{\text{cb}}$ in Figs. 5(b), (c) and (d). The values of the cyclotron electron mass m_{CR} and radiative decay parameter Γ were further obtained from the calculated CR positions.

At low density, see Fig. 5(a), the transport width dominates, $\tau^{-1} \gg \Gamma$, whereas at high densities both contributions become comparable in magnitude. While the overall agreement obtained without fitting parameters is encouraging, we should mention that the used semiclassical description becomes less accurate at low densities corresponding to transitions between low-lying Landau levels. Here the electrodynamic effects are negligible, while the transport width is expected to be larger than $1/\tau$ due to Landau quantization effects [59]. In Fig. 5, one clearly distinguishes four CR lines corresponding to different inraband (B_{CR2} and $B_{\text{CR}}^{\text{cb}}$) and inter-band ($B_{\text{CR1}}$ and B_{CR3}) transitions between distinct Landau levels.

V. EDGE PHOTOCURRENT AT CYCLOTRON RESONANCE IN CLASSICAL REGIME

In this section we discuss the model describing cyclotron resonance in the dc edge current. Edge photocurrent induced by terahertz radiation at zero and low magnetic fields far from the cyclotron resonance conditions was studied in bilayer graphene in our previous work [41]. It was shown that the dc edge current is induced by the high-frequency electric field of the incident THz radiation due to the breaking of the parity symmetry at the

U_g^{eff} [V]	n [10^{11} cm^{-2}]	B_{CR} [T]	m_{CR}/m_0	Γ [ps^{-1}]
0.5	0.23	$B_{\text{CR2}} = 1.8$	0.020	0.06
9.5	4.37	$B_{\text{CR}}^{\text{cb}} = 2.1$	0.023	1.00
15	6.90	$B_{\text{CR}}^{\text{cb}} = 2.4$	0.026	1.40
20	9.20	$B_{\text{CR}}^{\text{cb}} = 2.7$	0.029	1.70

TABLE I: Cyclotron resonance magnetic fields B_{CR2} and $B_{\text{CR}}^{\text{cb}}$, calculated cyclotron masses m_{CR}/m_0, and radiative decay parameter Γ obtained for different gate voltages U_g^{eff}. The values together with the transport width of the CR given by the momentum relaxation rate $1/\tau = 1.43$ ps^{-1} are used for calculating curves in Fig. 5.
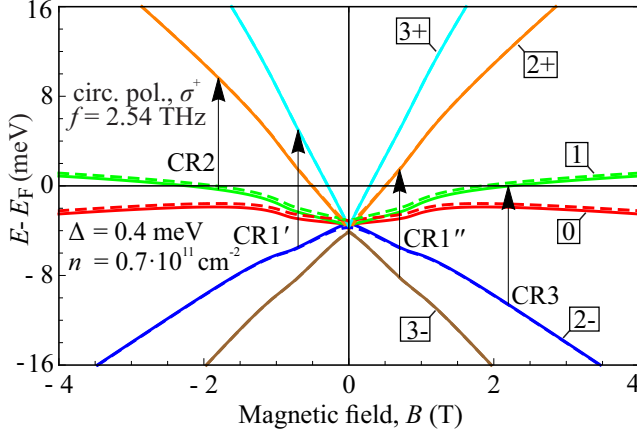

FIG. 7: Calculated Landau levels as a function of magnetic field for gate induced doping $n = 0.7 \cdot 10^{11}$cm^{-2} corresponding to bilayer asymmetry gap $\Delta = 0.4$ meV. The levels are labeled according to Eqs. (2). Solid/dashed lines correspond to valleys K^+/K^-. Arrows indicate allowed optical transitions for right circularly polarized radiation (σ^+) with $f = 2.54$ THz. Transitions labeled CR1′, CR1″, CR2, and CR3 correspond to experimentally observed resonances, see, e.g., Fig. 2. Due to close positions of CR1′ and CR1″ these resonances are not resolved in experiments, therefore, in the corresponding experimental plots they are labeled as CR1. Note that for linear polarized radiation used in experiments the resonances plotted at positive (negative) magnetic fields appear also at negative (positive) B.

edge. This phenomenon can be viewed as a dc conversion of the bulk ac electric current at the edge. Two possible microscopic mechanisms of such an ac-dc conversion were discussed. The first one is based on the alignment of the free carrier momenta by the high-frequency electric field and subsequent scattering of the carriers at the edge. The second one is related to the dynamic charge accumulation near the edge and synchronized charge motion along the edge. In line with Ref. [41] the dc edge voltage observed in the present work at low magnetic field behaves as $U \propto \sin(2\alpha + \varphi_B)$, where φ_B is the phase shift induced by magnetic field.

In the current work we present the theory of the edge photocurrent at high magnetic fields satisfying the cy-

clotron resonance condition, when the driving frequency ω is close to the cyclotron frequency ω_c. As seen in Figs. 2 and 6, the polarization and magnetic-field dependences of the edge photovoltage in the CR regime differ significantly from those at zero or low magnetic field addressed above. The sign of the voltage no longer depends on the orientation of the electric field with respect to the edge, see Ref. [41], but is defined by the direction of magnetic field.

Such a behaviour can be explained by the following model, see Fig. 8. Here, we discuss the model for positively charged holes, however its generalization for electrons is straightforward. At $\omega_c \tau \gg 1$ the holes in the 2D layer move along cyclotron orbits. When the frequency of the driving electric field coincides with the cyclotron frequency, the motion of holes becomes synchronized. The integral velocity of holes in the bulk of the 2D plane $\boldsymbol{v}_{\text{bulk}}$ rotates following the rotating electric field $\boldsymbol{E}$ of the incident wave. The oscillating electric field also leads to periodic accumulation and depletion of holes at the edge, however the hole density oscillates with a $\pi/2$ retardation as compared to electric field. This fact follows from the continuity equation $\partial n/\partial t + \partial i_x/\partial x = 0$, where n is the hole density and i_x is the hole flux normal to the edge. One may say, that the oscillations of the hole density at the edge are driven by the electric field $\tilde{\boldsymbol{E}}$, which is shifted by a quarter of period in time with respect to $\boldsymbol{E}$. Due to holes accumulation and depletion the integral hole velocity near the edge $\boldsymbol{v}_{\text{edge}}$ differs from $\boldsymbol{v}_{\text{bulk}}$. In the first half-period of the electric-field oscillations, when $E_y > 0$, the retarded field $\tilde{\boldsymbol{E}}$ points towards the edge leading to accumulation of holes at the edge and, consequently, to $|\boldsymbol{v}_{\text{edge}}| > |\boldsymbol{v}_{\text{bulk}}|$. At the second half-period, when $E_y < 0$, $\tilde{\boldsymbol{E}}$ points towards the bulk leading to depletion of holes at the edge, and during that time period $|\boldsymbol{v}_{\text{edge}}| < |\boldsymbol{v}_{\text{bulk}}|$. Such asymmetric oscillations of $\boldsymbol{v}_{\text{edge}}$ result in a net dc current flowing along the edge. This current is formed near the edge within a strip of the width equal to the diameter of the cyclotron orbit $l_c = 2v/|\omega_c|$. As seen in Fig. 8, the direction of this current is determined by the direction of the cyclotron motion, and hence, by the sign of the magnetic field. The model suggests, that the increase of the edge current at the cyclotron resonance is related to the increase of $\boldsymbol{v}_{\text{bulk}}$ and $\boldsymbol{v}_{\text{edge}}$ due to resonant absorption.

The discussed mechanism describes the formation of the edge current at classical magnetic fields, when $\varepsilon_F/\hbar \gg |\omega_c|$, where ε_F is the Fermi energy. It is valid for intra-band absorption at high carrier densities, see the observed $B_{\text{CR}}^{\text{cb}}$ resonance in Fig. 5 (b-d). Resonances CR1 and CR3 are caused by inter-band transitions between valence and conduction band Landau levels and formation of the edge current in that case should be considered separately [39].

For microscopic description of the edge photocurrent we apply the Boltzmann approach, which is valid for the
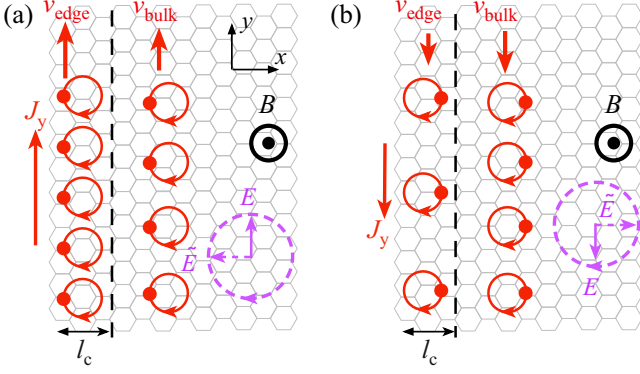
FIG. 8: Schematic illustration of the edge current formation in the cyclotron resonance regime considering positively charged holes and circularly polarized radiation. Charge carriers move along cyclotron orbits. In the bulk the integral velocity of carriers $\boldsymbol{v}_{\text{bulk}}$ rotates following rotating electric field $\boldsymbol{E}$ of radiation. The oscillating electric field leads to dynamic carrier accumulation and depletion at the edge, however the carrier density oscillates with a $\pi/2$ retardation as compared to $\boldsymbol{E}$ (one can say, that carrier density oscillations are driven by the electric field in the past $\tilde{\boldsymbol{E}}$). Due to the density oscillations the absolute value of the integral carrier velocity near the edge $\boldsymbol{v}_{\text{edge}}$ is different at first [$E_y > 0$, panel (a)] and second [$E_y < 0$, panel (b)] half-periods of the electric field oscillations, resulting in a net dc current flowing along the edge.

classical range of the driving field frequency $\omega \ll \varepsilon_F/\hbar$, corresponding to intra-band absorption of the incident radiation. We consider a semi-infinite 2D gas of charge carriers occupying $x \geq 0$ half-space. The distribution function of the charge carriers (electrons or holes) $f(\boldsymbol{p}, x, t)$ is found from the Boltzmann kinetic equation

$$\frac{\partial f}{\partial t} + v_x \frac{\partial f}{\partial x} + e\left(\boldsymbol{\mathcal{E}}(x,t) + \frac{1}{c}\boldsymbol{v}\times\boldsymbol{B}\right)\cdot\frac{\partial f}{\partial \boldsymbol{p}} = -\frac{f - \langle f\rangle}{\tau}, \tag{5}$$

where $\boldsymbol{\mathcal{E}}(x,t) = \boldsymbol{\mathcal{E}}(x)\exp(-\mathrm{i}\omega t) + \text{c.c.}$ is the total electric field in the sample consisting of the ac field of the incident wave $\boldsymbol{E}\exp(-\mathrm{i}\omega t) + \text{c.c.}$ and the local screening field due to redistribution of charge, $\boldsymbol{B} \parallel z$ is the magnetic field, $\boldsymbol{p}$ and $\boldsymbol{v} = \boldsymbol{p}/m$ are the carrier momentum and velocity, respectively, $\langle f\rangle$ is the distribution function averaged over directions of $\boldsymbol{p}$, τ is the relaxation time, e is the carrier electric charge and m is the effective mass. In what follows we assume that τ is independent of carrier energy. The kinetic equation should be supplemented with a boundary condition at $x = 0$. Here we consider the specular reflection of carriers at the sample edge implying that the distribution function satisfies $f(p_x, p_y, 0) = f(-p_x, p_y, 0)$.

Equation (5) is solved by expanding the distribution function in a series over the electric field $\boldsymbol{E}$ as $f(\boldsymbol{p}, x, t) = f_0(\boldsymbol{p}, x) + [f_1(\boldsymbol{p}, x)\exp(-\mathrm{i}\omega t) + \text{c.c.}] + f_2(\boldsymbol{p}, x)$, where f_0 is the equilibrium distribution function, $f_1 \propto E$ and

$f_2 \propto EE^*$ [33]. The density of the dc edge current is determined by the time-independent correction $f_2(\boldsymbol{p}, x)$ and reads

$$j_y(x) = 4e\sum_{\boldsymbol{p}} v_y f_2(\boldsymbol{p}, x), \tag{6}$$

where the factor 4 accounts for the spin and valley degeneracy. Using Eq. (5) one can present $j_y(x)$ as [41]

$$j_y(x) = -4e\tau\sum_{\boldsymbol{p}} v_x v_y \frac{\partial f_2}{\partial x} + 4\frac{e^2\tau}{m}\sum_{\boldsymbol{p}}(E_y^* f_1 + E_y f_1^*). \tag{7}$$

To calculate $j_y(x)$ using Eq. (7) one needs to find $f_1(\boldsymbol{p}, x)$ and $f_2(\boldsymbol{p}, x)$ from Eq. (5), which can be done numerically. However, as shown in Ref. [41], the total current flowing along the edge $J_y = \int_0^\infty j_y(x)dx$ is found analytically and can be expressed in terms of the conductivity tensor. Substituting the expression for the conductivity tensor in Eq. (13) of Ref. [41] and setting $\tau_1 = \tau_2 \equiv \tau$ we obtain

$$J_y = \frac{e\tau^2\sigma_0}{m}\Big[\mathcal{A}|\boldsymbol{E}|^2 + \mathrm{i}\mathcal{B}(E_x E_y^* - E_y E_x^*)$$
$$+ \mathcal{C}(E_x E_y^* + E_y E_x^*) + \mathcal{D}(|E_x|^2 - |E_y|^2)\Big], \tag{8}$$

where

$$\mathcal{A} = \frac{2\omega_c\tau}{1 + 2(\omega^2 + \omega_c^2)\tau^2 + (\omega^2 - \omega_c^2)^2\tau^4}, \tag{9}$$

$$\mathcal{B} = -\frac{1 + (\omega^2 + \omega_c^2)\tau^2}{\omega\tau\left[1 + 2(\omega^2 + \omega_c^2)\tau^2 + (\omega^2 - \omega_c^2)^2\tau^4\right]},$$

$$\mathcal{C} = -\frac{1 + (\omega^2 - 5\omega_c^2)\tau^2}{(1 + 4\omega_c^2\tau^2)[1 + 2(\omega^2 + \omega_c^2)\tau^2 + (\omega^2 - \omega_c^2)^2\tau^4]},$$

$$\mathcal{D} = \frac{2\omega_c\tau\left[2 + (\omega^2 - \omega_c^2)\tau^2\right]}{(1 + 4\omega_c^2\tau^2)[1 + 2(\omega^2 + \omega_c^2)\tau^2 + (\omega^2 - \omega_c^2)^2\tau^4]}.$$

Here σ_0 is the conductivity of 2D electron (or hole) gas at zero magnetic field, and $\omega_c = eB_z/(m_{\text{CR}}c)$ is the cyclotron frequency. As follows from Eq. (9), the dc edge current in presence of a magnetic field is induced by linearly polarized radiation with nonzero terms $E_x E_y^* + E_y E_x^*$ or $|E_x|^2 - |E_y|^2$, circularly polarized radiation with nonzero $\mathrm{i}(E_x E_y^* - E_y E_x^*)$, and also unpolarized radiation.

Let us now consider the behaviour of the edge photocurrent (8) in the vicinity of the cyclotron resonance, i.e. in the frequency range $|\omega - |\omega_c|| \ll |\omega_c|$ and $|\omega_c|\tau \gg 1$. For linearly polarized radiation the edge current is determined by the first, third, and fourth terms in Eq. (8). The cyclotron resonance occurs for both directions of magnetic field at $B_z = \pm B_{\text{CR}}$, where $B_{\text{CR}} = m_{\text{CR}}\omega c/|e|$. Near the resonance the edge current given by Eqs. (8)

and (9) is simplified to

$$J_y^{\text{lin}} = \frac{\text{sign}(B_z)c\tau\eta I}{2B_{\text{CR}}}$$
$$\times \left[1 + \frac{\sqrt{1 + (\omega - |\omega_c|)^2\tau^2}}{2|\omega_c|\tau} \sin(2\alpha + \theta_B) \right] . \quad (10)$$

Here α is the electric field angle with respect to the edge,

$$\eta = \frac{2\pi\sigma_0}{n_\omega c} \frac{1}{1 + (\omega - |\omega_c|)^2\tau^2} \quad (11)$$

is the absorbance of the 2D layer in the vicinity of cyclotron resonance and far from the edge for non-polarized radiation, $I = cn_\omega|\boldsymbol{E}|^2/(2\pi)$ is the intensity of the radiation, and n_ω is the refractive index of the dielectric medium surrounding bilayer graphene. The phase shift θ_B is determined from

$$\tan\theta_B = \frac{1 + |\omega_c|(\omega - |\omega_c|)\tau^2}{\omega_c\tau} . \quad (12)$$

The sign, magnitude and polarization dependence of the edge dc current given by Eqs. (10) and (11) are in agreement with experimental observations, shown in Figs. 2, 3, and 6. Equations (10) and (11) show that the edge dc current at cyclotron resonance is proportional to the absorbed energy. Therefore, an increase of the edge current magnitude at cyclotron resonance is due to the increase of absorption. The direction of the edge current is determined by the direction of magnetic field in agreement with experimental data in Figs. 2 and 3, which show the change of the photovoltage sign for opposite directions of the magnetic field. Interestingly, the direction of the dc current is the same for electrons and holes. These characteristic features are similar to the ones observed for the edge photocurrent at strong magnetic field under conditions of the quantum Hall effect [39].

As follows from Eq. (10), the edge current induced by linearly polarized radiation consists of a polarization-independent contribution and a contribution $\propto \sin(2\alpha + \theta_B)$ that is sensitive to the direction of the electric field. The second contribution $\sim |\omega_c|\tau$ is less than the first one. The phase shift θ_B, given by Eq. (12), vanishes at the resonance so that the polarization dependent part of J_y^{lin} behaves as $\sin 2\alpha$. Weak dependence of the edge current on polarization and $\sin 2\alpha$ behaviour are in line with experimental observations shown in Fig. 6. Far from resonance, when $|\omega - |\omega_c||\tau \gg 1$, we have $|\theta_B| = \pi/2$, so that the polarization dependent part of J_y^{lin} behaves as $\cos 2\alpha$.

For circularly polarized radiation the edge photocurrent is determined by the first two terms in Eq. (8). The cyclotron resonance occurs for a particular direction of the magnetic field at $B_z = -(e/|e|)P_{\text{circ}}B_{\text{CR}}$, where $P_{\text{circ}} = i(E_xE_y^* - E_yE_x^*)/|\boldsymbol{E}|^2$, $P_{\text{circ}} = \pm 1$ for right (left)-hand circularly polarized radiation. Near the resonance
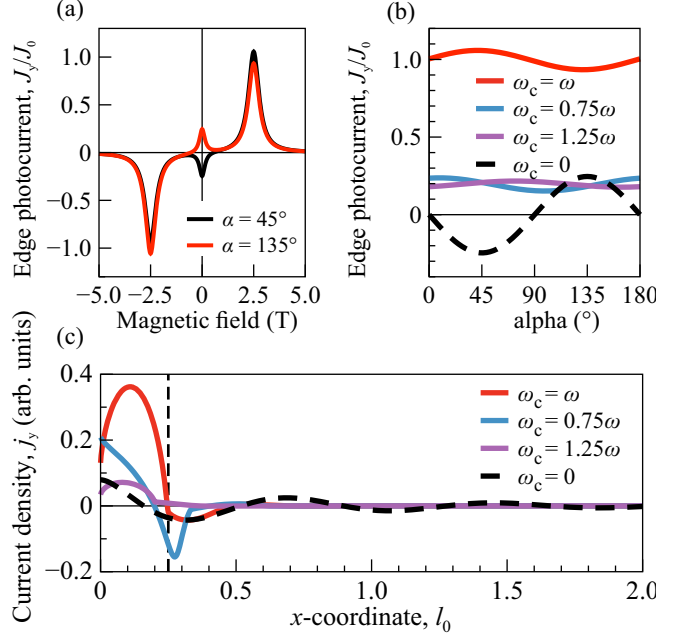

FIG. 9: (a) Edge photocurrent calculated after Eqs. (8) and (9) for linearly polarized radiation with $(E_xE_y^* + E_yE_x^*)/|\boldsymbol{E}|^2 = \pm 1$. Cyclotron resonances occur at $B_z = \pm 2.4$ T. (b) Dependence of the edge current on the azimuthal angle at different magnetic fields – in resonance, $\omega_c = \omega$ (red line), and out of resonance, $\omega_c = 0.85\,\omega$, $\omega_c = 1.15\,\omega$. The curve at zero magnetic field is shown by dashed line for comparison. (c) Distribution of the edge current density over x-coordinate for circularly polarized incident radiation. The dashed vertical line shows the diameter of the cyclotron orbit $l_c = 2l_0/(\omega_c\tau)$ at resonance, l_0 is the mean free path length. The parameters used are: $\omega/(2\pi) = 2.54$ THz, $\tau = 0.7$ ps, $B_{\text{CR}} = 2.4$ T and $\omega\tau = 11$, $J_0 = c\tau\eta I/(2B_{\text{CR}})$.

Eq. (8) yields

$$J_y^{\text{circ}} = \frac{\text{sign}(B_z)c\tau\eta I}{B_{\text{CR}}} . \quad (13)$$

Figure 9(a) shows the edge photocurrent calculated after Eqs. (8) and (9) as a function of the magnetic field. The calculations were done for two linear polarizations $(E_xE_y^* + E_yE_x^*)/|\boldsymbol{E}|^2 = \pm 1$, corresponding to $\alpha = 45°$ and $135°$. Parameters used in calculations are the same as in calculations of the dashed curve in Fig. 5(c), see $U_g^{\text{eff}} = 15$ V in Tab. I. Sharp CR resonances in the edge current occur at $B_z = \pm 2.4$ T with magnitude, which is almost independent of the polarization, and sign, which is determined by the direction of magnetic field. These results are in good agreement with experimental observations, see Figs. 2, 3 and 5. By contrast, the directions of the dc current at $B_z = 0$ is opposite for $\alpha = 45°$ and $135°$, see Ref. [41]. The dependence of J_y on α is shown in Fig. 9(b) for different values of B_z corresponding to the resonances CR2 and CR3. Note that the dependencies are presented for low densities corresponding to CRs

in the quantum mechanical limit, because at higher densities the SdH make it difficult extraction of the CR's amplitude and, consequently, do not allow to analyze its polarization dependence. Nevertheless, it is clear that the polarization dependence of the edge photocurrent at CR is indeed very weak and follows $\sin 2\alpha$ dependence, whereas out of the resonance the polarization dependence of J_y changes to $\cos 2\alpha$ (see Ref. [41]), being in line with Eq. (10). The distribution of the edge photocurrent density $j_y(x)$, calculated after Eq. (7) with $f_1(\boldsymbol{p}, x)$ found numerically from Eq. (5), is shown in Fig. 9(c). The results are obtained for circularly polarized radiation when the first term is Eq. (7) vanishes. It is seen that at $\omega_c \tau \gg 1$ the dc current flows mainly in the strip of the width equal to the cyclotron diameter $l_c = 2l_0/(\omega_c\tau)$, which at this conditions is much less than the mean free path l_0. By contrast, at zero magnetic field the current is distributed over a much larger length $\sim l_0$.

VI. SUMMARY

We reported on the observation and study of cyclotron resonance induced edge currents in high mobility hBN encapsulated bilayer graphene. The cyclotron masses, momentum relaxation time, and carrier densities determined from the position and shape of CR together with the analysis of $1/B$-periodic magnetooscillations demonstrate that in studied samples and for the investigated carrier density range these parameters do not distinguish from those of the material bulk. Experimental findings for high carrier densities corresponding to the semiclassical regime are explained within the microscopic model based on the Boltzmann kinetic equation. Theoretical model describing the edge photocurrent at low carrier density, when the cyclotron resonance emerges due to inter-band or intra-band transitions between the lowest Landau levels, is a future task.

VII. ACKNOWLEDGMENTS

[1] K. v. Klitzing, G. Dorda, and M. Pepper, Phys. Rev. Lett. **45**, 494 (1980).

[2] B. I. Halperin, Phys. Rev. B **25**, 2185 (1982).

[3] S. D. Sarma and A. Pinczuk, *Perspectives in Quantum Hall Effects* (John Wiley and Sons, New York, 1997).

[4] K. S. Novoselov, E. McCann, S. V. Morozov, V. I. Fal'ko, M. I. Katsnelson, U. Zeitler, D. Jiang, F. Schedin, and A. K. Geim, Nat. Phys. **2**, 177 (2006).

[5] A. H. C. Neto, F. Guinea, N. M. R. Peres, K. S. Novoselov, and A. K. Geim, Rev. Mod. Phys. **81**, 109 (2009).

[6] S. Murakami, N. Nagaosa, and S.-C. Zhang, Phys. Rev. Lett. **93**, 156804 (2004).

[7] C. L. Kane and E. J. Mele, Phys. Rev. Lett. **95**, 146802 (2005).

[8] B. A. Bernevig and S.-C. Zhang, Phys. Rev. Lett. **96**, 106802 (2006).

[9] M. König, S. Wiedmann, C. Brune, A. Roth, H. Buhmann, L. W. Molenkamp, X.-L. Qi, and S.-C. Zhang, Science **318**, 766 (2007).

[10] M. Z. Hasan and C. L. Kane, Rev. Mod. Phys. **82**, 3045 (2010).

[11] X.-L. Qi and S.-C. Zhang, Rev. Mod. Phys. **83**, 1057 (2011).

[12] I. Martin, Y. M. Blanter, and A. F. Morpurgo, Phys. Rev. Lett. **100**, 036804 (2008).

[13] W. Yao, S. A. Yang, and Q. Niu, Phys. Rev. Lett. **102**, 096801 (2009).

[14] F. Zhang, J. Jung, G. A. Fiete, Q. Niu, and A. H. MacDonald, Phys. Rev. Lett. **106**, 156801 (2011).

[15] J. Jung, F. Zhang, Z. Qiao, and A. H. MacDonald, Phys. Rev. B **84**, 075418 (2011).

[16] A. Vaezi, Y. Liang, D. H. Ngai, L. Yang, and E.-A. Kim, Phys. Rev. X **3**, 021018 (2013).

[17] J. D. Sanchez-Yamagishi, J. Y. Luo, A. F. Young, B. M. Hunt, K. Watanabe, T. Taniguchi, R. C. Ashoori, and P. Jarillo-Herrero, Nat. Nanotechnol. **12**, 118 (2016).

[18] Y. Niimi, T. Matsui, H. Kambara, K. Tagami, M. Tsukada, and H. Fukuyama, Phys. Rev. B **73**, 085421 (2006).

[19] K. A. Ritter and J. W. Lyding, Nat. Mater. **8**, 235 (2009).

[20] L.-J. Yin, H. Jiang, J.-B. Qiao, and L. He, Nat. Commun. **7**, 11760 (2016).

[21] C. Casiraghi, A. Hartschuh, H. Qian, S. Piscanec, C. Georgi, A. Fasoli, K. S. Novoselov, D. M. Basko, and A. C. Ferrari, Nano Lett. **9**, 1433 (2009).

[22] S. Heydrich, M. Hirmer, C. Preis, T. Korn, J. Eroms, D. Weiss, and C. Schüller, Appl. Phys. Lett. **97**, 043113 (2010).

[23] M. Begliarbekov, O. Sul, S. Kalliakos, E.-H. Yang, and S. Strauf, Appl. Phys. Lett. **97**, 031908 (2010).

[24] K. C. Nowack, E. M. Spanton, M. Baenninger, M. König, J. R. Kirtley, B. Kalisky, C. Ames, P. Leubner, C. Brüne, H. Buhmann, et al., Nat. Mater. **12**, 787 (2013).

[25] A. Marguerite, J. Birkbeck, A. Aharon-Steinberg, D. Halbertal, K. Bagani, I. Marcus, Y. Myasoedov, A. K. Geim, D. J. Perello, and E. Zeldov, Nature **575**, 628 (2019).

[26] M. Slota, A. Keerthi, W. K. Myers, E. Tretyakov, M. Baumgarten, A. Ardavan, H. Sadeghi, C. J. Lambert, A. Narita, K. Müllen, et al., Nature **557**, 691 (2018).

[27] Z. Liu, K. Suenaga, P. J. F. Harris, and S. Iijima, Phys.

Rev. Lett. **102**, 015501 (2009).

[28] L. Ju, Z. Shi, N. Nair, Y. Lv, C. Jin, J. Velasco, C. Ojeda-Aristizabal, H. A. Bechtel, M. C. Martin, A. Zettl, et al., Nature **520**, 650 (2015).

[29] Z. Fei, M. D. Goldflam, J.-S. Wu, S. Dai, M. Wagner, A. S. McLeod, M. K. Liu, K. W. Post, S. Zhu, G. C. A. M. Janssen, et al., Nano Lett. **15**, 8271 (2015).

[30] L. Jiang, Z. Shi, B. Zeng, S. Wang, J.-H. Kang, T. Joshi, C. Jin, L. Ju, J. Kim, T. Lyu, et al., Nat. Mater. **15**, 840 (2016).

[31] A. Y. Nikitin, P. Alonso-González, S. Vélez, S. Mastel, A. Centeno, A. Pesquera, A. Zurutuza, F. Casanova, L. E. Hueso, F. H. L. Koppens, et al., Nat. Photonics **10**, 239 (2016).

[32] P. Li, I. Dolado, F. J. Alfaro-Mozaz, A. Y. Nikitin, F. Casanova, L. E. Hueso, S. Vélez, and R. Hillenbrand, Nano Lett. **17**, 228 (2016).

[33] J. Karch, C. Drexler, P. Olbrich, M. Fehrenbacher, M. Hirmer, M. M. Glazov, S. A. Tarasenko, E. L. Ivchenko, B. Birkner, J. Eroms, et al., Phys. Rev. Lett. **107**, 276601 (2011).

[34] M. Glazov and S. Ganichev, Phys. Rep. **535**, 101 (2014).

[35] K.-M. Dantscher, D. A. Kozlov, M. T. Scherr, S. Gebert, J. Bärenfänger, M. V. Durnev, S. A. Tarasenko, V. V. Bel'kov, N. N. Mikhailov, S. A. Dvoretsky, et al., Phys. Rev. B **95**, 201103(R) (2017).

[36] M. Luo and Z. Li, Phys. Rev. B **96**, 165424 (2017).

[37] S. D. Ganichev, D. Weiss, and J. Eroms, Ann. Phys. **529**, 1600406 (2017).

[38] S.-Y. Xu, Q. Ma, H. Shen, V. Fatemi, S. Wu, T.-R. Chang, G. Chang, A. M. M. Valdivia, C.-K. Chan, Q. D. Gibson, et al., Nat. Phys. **14**, 900 (2018).

[39] H. Plank, M. V. Durnev, S. Candussio, J. Pernul, K.-M. Dantscher, E. Mönch, A. Sandner, J. Eroms, D. Weiss, V. V. Bel'kov, et al., 2D Mater. **6**, 011002 (2018).

[40] M. V. Durnev and S. A. Tarasenko, Ann. Phys. **531**, 1800418 (2019).

[41] S. Candussio, M. V. Durnev, S. A. Tarasenko, J. Yin, J. Keil, Y. Yang, S.-K. Son, A. Mishchenko, H. Plank, V. V. Bel'kov, et al., Phys. Rev. B **102**, 045406 (2020).

[42] M. Otteneder, S. Hubmann, X. Lu, D. A. Kozlov, L. E.

[43] Golub, K. Watanabe, T. Taniguchi, D. K. Efetov, and S. D. Ganichev, Nano Lett. **20**, 7152 (2020).

[43] Z. D. Kvon, S. N. Danilov, N. N. Mikhailov, S. A. Dvoretsky, and S. D. Ganichev, **40**, 1885 (2008).

[44] P. Olbrich, C. Zoth, P. Vierling, K.-M. Dantscher, G. V. Budkin, S. A. Tarasenko, V. V. Bel'kov, D. A. Kozlov, Z. D. Kvon, N. N. Mikhailov, et al., Phys. Rev. B **87**, 235439 (2013).

[45] P. Olbrich, J. Kamann, M. König, J. Munzert, L. Tutsch, J. Eroms, D. Weiss, M.-H. Liu, L. E. Golub, E. L. Ivchenko, et al., Phys. Rev. B **93**, 235439 (2016).

[46] J. C. Slonczewski and P. R. Weiss, Phys. Rev. **109**, 272 (1958).

[47] J. W. McClure, Phys. Rev. **108**, 612 (1957).

[48] M. S. Dresselhaus and G. Dresselhaus, Adv. Phys. **51**, 1 (2002).

[49] E. McCann and V. I. Fal'ko, Phys. Rev. Lett. **96**, 086805 (2006).

[50] E. McCann and M. Koshino, Rep. Prog. Phys. **76**, 056503 (2013).

[51] S. Slizovskiy, A. Garcia-Ruiz, N. Drummond, and V. I. Falko, arXiv:1912.10067 (2019).

[52] M. Mucha-Kruczyński, E. McCann, and V. I. Fal'ko, Semicond. Sci. Technol. **25**, 033001 (2010).

[53] D. S. L. Abergel and V. I. Fal'ko, Phys. Rev. B **75**, 155430 (2007).

[54] P. G. Silvestrov and K. B. Efetov, Phys. Rev. B **77**, 155436 (2008).

[55] S. Slizovskiy and V. I. Fal'ko, Phys. Rev. B **97**, 075404 (2018).

[56] V. I. Fal'ko and D. E. Khmel'nitskii, Sov. Phys. JETP **68**, 1150 (1989).

[57] S. A. Mikhailov, Phys. Rev. B **70**, 165311 (2004).

[58] T. Herrmann, I. A. Dmitriev, D. A. Kozlov, M. Schneider, B. Jentzsch, Z. D. Kvon, P. Olbrich, V. V. Bel'kov, A. Bayer, D. Schuh, et al., Phys. Rev. B **94**, 081301 (2016).

[59] I. A. Dmitriev, A. D. Mirlin, D. G. Polyakov, and M. A. Zudov, Rev. Mod. Phys. **84**, 1709 (2012).